Princeton Plasma Physics Laboratory

PPPL-

PPPL-

Princeton Plasma Physics Laboratory
Report Disclaimers

Full Legal Disclaimer

This report was prepared as an account of work sponsored by an agency of the United States Government. Neither the United States Government nor any agency thereof, nor any of their employees, nor any of their contractors, subcontractors or their employees, makes any warranty, express or implied, or assumes any legal liability or responsibility for the accuracy, completeness, or any third party's use or the results of such use of any information, apparatus, product, or process disclosed, or represents that its use would not infringe privately owned rights. Reference herein to any specific commercial product, process, or service by trade name, trademark, manufacturer, or otherwise, does not necessarily constitute or imply its endorsement, recommendation, or favoring by the United States Government or any agency thereof or its contractors or subcontractors. The views and opinions of authors expressed herein do not necessarily state or reflect those of the United States Government or any agency thereof.

Trademark Disclaimer

Reference herein to any specific commercial product, process, or service by trade name, trademark, manufacturer, or otherwise, does not necessarily constitute or imply its endorsement, recommendation, or favoring by the United States Government or any agency thereof or its contractors or subcontractors.

PPPL Report Availability

Princeton Plasma Physics Laboratory:

http://www.pppl.gov/techreports.cfm

Office of Scientific and Technical Information (OSTI):

http://www.osti.gov/bridge

Related Links:

U.S. Department of Energy

Office of Scientific and Technical Information

Fusion Links

NSTX report on FES Joint Facilities Research Milestone 2010

by R. Maingi, J-W. Ahn, T.K. Gray, A.G. McLean, V.A. Soukhanovskii

Annual Target: Conduct experiments on major fusion facilities to improve understanding of the heat transport in the tokamak scrape-off layer (SOL) plasma, strengthening the basis for projecting divertor conditions in ITER. The divertor heat flux profiles and plasma characteristics in the tokamak scrape-off layer will be measured in multiple devices to investigate the underlying thermal transport processes. The unique characteristics of C-Mod, DIII-D, and NSTX will enable collection of data over a broad range of SOL and divertor parameters (e.g., collisionality ν^*, beta β, parallel heat flux $q_\parallel$, and divertor geometry). Coordinated experiments using common analysis methods will generate a data set that will be compared with theory and simulation.

Quarter 4 Milestone

Complete necessary experiments, data analysis and associated interpretive modeling. Prepare a joint report on the empirical understanding gained, the connections to edge transport models, and the opportunities for more detailed and extensive comparisons to theory and simulation. Identify critical research areas to improve extrapolation to ITER.

Completion of 4th Quarter Milestone – Executive Summary for NSTX

The targeted goal for the fourth quarter was achieved, as documented in the remainder of the joint report. All three devices find that the mapped heat flux width λ_q^{mid} varied with plasma current $I_p^{-\alpha}$, with the weakest dependence in C-Mod Enhanced D_α H-mode (α=0.17), and stronger dependences in C-Mod L-modes, and DIII-D and NSTX H-modes (all $\alpha \geq 1$). In addition, all three devices show no dependence of λ_q^{mid} on power into the scrape-off layer (SOL) or toroidal field.

The trends above in NSTX were documented in ELMy H-modes, and then confirmed qualitatively in ELM-free H-modes with lithium conditioning. A portion of these results were modeled with the XGC-0 and the SOLT codes (described in the full report), suggesting the importance of neoclassical transport scaling, and X-point effects, and turbulent cross-field transport in the SOL. For ITER, confirmation and understanding of the I_p scaling is identified as a critical step for divertor projections.

N1. Introduction

Power is input into tokamaks via a variety of techniques, including neutral beam injection, radiofrequency heating, and resistive or ohmic heating, with the goal of simulating certain aspects of the conditions needed for thermonuclear fusion. In steady state, this power must be exhausted by the plasma facing components (PFC). Technology has progressed to enable steady heat flux removal up to 10 MW/m^2, including the ability to handle limited transients above that value. These heat fluxes are quite high: as a point of reference, rocket nozzles typically experience heat fluxes in the range of 1 MW/m^2.

The magnetic divertor concept used in fusion devices channels the power to PFCs that are specially designed to handle both the steady heat flux, and transients due to instabilities, such as Edge Localized Modes (ELMs)[1] and disruptions. The magnetic divertor has an additional benefit in that it facilitates access to an improved energy confinement regime known as H-mode. However the divertor also tends to concentrate power in a relatively narrow region known as the divertor target. The plama intercepts the divertor target in two geometrically separated regions: the outer and inner strike points (e.g. see Figure N1-1). For geometric and transport reasons, the outer strike point, i.e. the leg at larger major radius, tends to have higher heat flux than the inner strike point in tokamaks. Thus the focus of international research has been on characterization of the outer divertor

Figure N1-1: Equilibrium reconstruction for a low δ discharge (shot# 132341, 0.41 s) with δ ~ 0.44, κ = 2.1 and f_{exp} = 4. The inner and outer strike points are labeled as A and B.

heat flux, partly to improve the projection for next step device, such as ITER.

Peak heat fluxes of magnitude ~ 10 MW/m^2 are predicted at the outer strike point in the ITER, based on 2-D calculations of the edge plasma and neutral gas transport[2-4]. Those calculations[5] assume that the transport along the magnetic field is mostly classical,
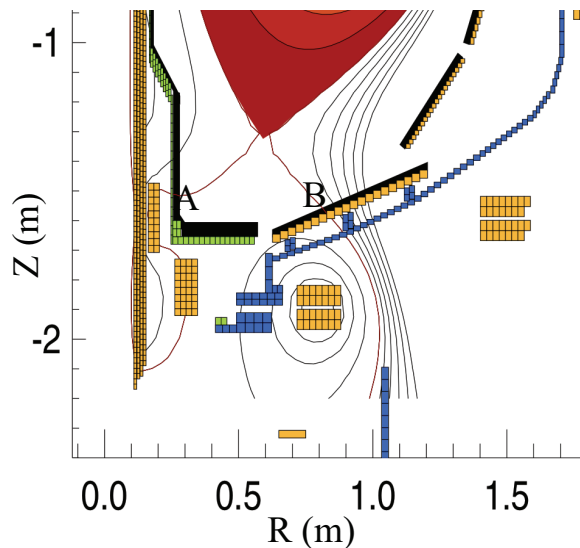
with some modifications for kinetic effects, while transport across the field is governed by anomalous diffusion, characterized by fixed transport coefficients. The magnitude of those transport coefficients is based on values needed to simulate existing devices. However analysis of present experiments points to a wide range for those cross-field transport coefficients, leading to considerable uncertainty about the expected width or footprint of the heat flux profile[6].

Multi-machine studies have been conducted to experimentally determine the scaling of the divertor heat flux width mapped to the midplane, as well as the electron temperature profile widths measured directly at the midplane[7, 8]. These studies point to a major radius scaling of the temperature width, and the midplane heat flux width in the parallel direction, $\lambda_{q\parallel}^{mid}$ or λ_q for short, assuming that electron conduction dominates the power balance (e.g. Figure N1-2). However research in individual devices has pointed to several key parameters that affect the heat flux width, e.g. plasma current[9-11], I_p.

The heat flux profiles in the outer divertor typically have an exponential or offset exponential shape, with the characteristic scale length in the scrape-off layer (SOL)

Figure N1-2: Ratio of $\lambda_{q\parallel}^{mid}$ to machine major radius, R_0, as a function of separatrix density, n_{sep}, normalized by the Greewnwald density, n_{Green}. The value is computed as 2/7 λ_{Te}^{mid}, assuming electron conduction dominates parallel transport [B. Lipshultz, et al., Nucl. Fusion **47** (2007) 1189].

about 2-4 times longer than the scale falloff on the private flux region side, e.g. Figure N1-3. Note that the heat flux profiles in the inner divertor are often broad, due to a phenomenon known as partial detachment[12, 13]. Fitting the outer divertor profiles with exponential functions can make comparison across devices difficult, because of differing functional forms, error minimization schemes, etc. An alternate way to compare profiles
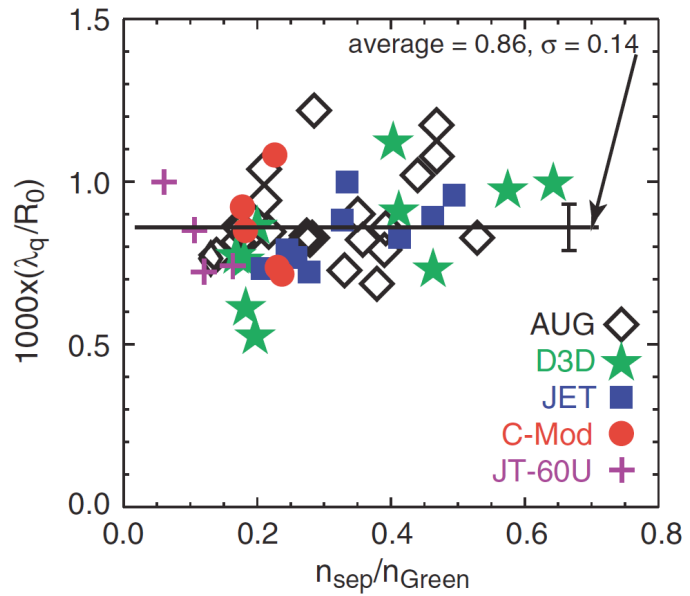
without the need for profile fitting is by using an integral definition of the divertor heat flux width[14] λ_q^{div}, which is given by:

$$\lambda_q^{div} = P_{div}^{out}/(2\pi r_{div}^{out} \times q_{div,peak}^{out})$$

where

P_{div}^{out} = total power incident on outer divertor

r_{div}^{out} = radius of peak heat flux

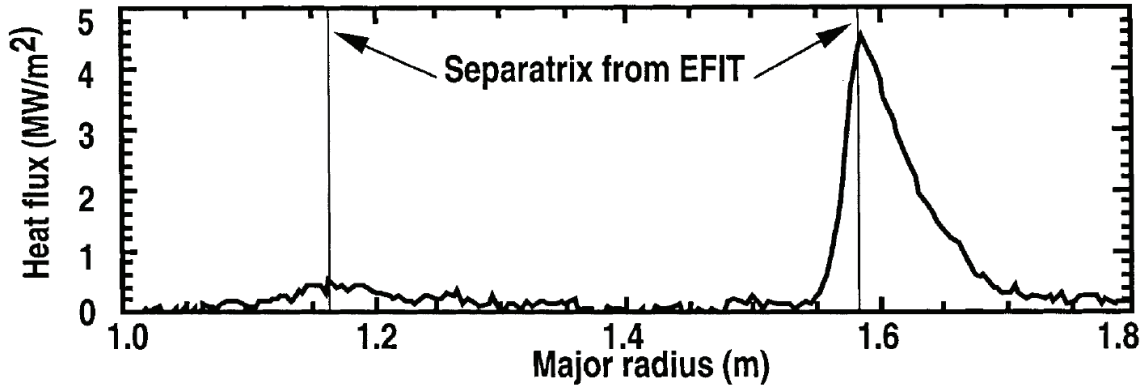$q_{div,peak}^{out}$ = outer divertor peak heat flux

Figure N1-3: typical plot of heat flux profiles from the inner and outer divertors in DIII-D. The two vertical lines represent the inner and outer strike points. The outer divertor heat flux is typically higher, whereas dissipative processes, such as radiation, charge exchange, and recombination, reduce the peak heat flux on the inner side [C.J. Lasnier, et al., Nucl. Fusion 38 (1998) 1225.

This λ_q^{div} can be easily to a characteristic scale length at the outer midplane λ_q^{mid} via the magnetic flux expansion f_{exp}, i.e.

$$\lambda_q^{mid} = \lambda_{q,div}^{out}/f_{exp}$$

where

$f_{exp} = r_{mid}B_\theta^{mid}/(r_{div}^{out}B_\theta^{div})$

$r_{mid} = r_{div}^{out}$ mapped to the midplane

B_θ^{mid} = midplane poloidal field strength

B_θ^{mid} = divertor poloidal field strength

Thus it was decided early in the research planning process to use λ_q^{mid} as defined above as the central way to compare data[15-18] across Alcator C-Mod, DIII-D, and NSTX. In NSTX, all the data presented are exclusively in H-mode.

In NSTX the scope of the experimental research effort was threefold. The first entailed diagnostic preparation to measure the heat flux profiles in the presence of lithium

wall conditioning, which complicates infrared (IR) interpretation. A fast IR camera installed in 2009 was upgraded to look at two different wavelength bands, as described in Section N2-2.

The second part involved detailed analysis of previous well-characterized sets of heat flux scaling experiments from 2004-2009 in terms of the midplane profile width. All of these data were obtained in ELMy discharges, mostly with small Type V ELMs, using an older 30 Hz IR camera. In 20008 and 2009, the datasets were obtained before lithium was applied as a wall coating technique, to facilitate interpretation of surface temperatures and heat fluxes from IR thermography. Much of this older dataset was obtained in low triangularity (δ) discharges. Analysis of the heat flux widths for this dataset is presented in Section N2-3.

The final part of NSTX research involved obtaining a comprehensive dataset in strongly shaped discharges with high δ and elongation, as these are of interest to NSTX-Upgrade (Design: I_P = 2 MA, B_t = 1 T, P_{NBI} = 10 MW, 5 sec pulse length) in particular and future spherical tokamaks in general. This involved fine scans in I_p, toroidal field B_t, neutral beam heating power P_{NBI}, radial separation between the two X-points at the outer midplane, δ_r^{sep}, and measurements in a poloidal cross-section shape that matches a scaled C-Mod and DIII-D shape[19, 20]. These data were obtained at two different lithium deposition rates, with the plasmas being more ELMy with the lower deposition rates, and the preliminary data analysis for these new datasets are given in Section N2-4.

For completeness, we also describe experiments in NSTX to reduce the peak heat flux by use of the innovative 'snowflake' divertor shape[21-23] in Section N2-5, as well as investigation of the effect of applied non-axisymmetric magnetic perturbations on heat flux profiles. Analysis of the effective heat flux widths in these experiments is still in progress, but we anticipate that when properly optimized, each will result in an increase in the heat flux width, and hence a decrease in the peak heat flux.

N2. Diagnostic preparations

Infrared (IR) thermography on NSTX was originally installed[24, 25] in 2002 to measure the surface temperature, from which the heat flux could be computed at a 30 Hz frame rate. In 2009, a fast IR camera was implemented[26] to allow measurement of the divertor heat flux carried by Edge Localized Modes (ELMs) in NSTX. This fast IR camera has a 128x128 pixel detector with 1.6 kHz full frame capture rate. It can be operated up to 6.3kHz, with a binned 96x32 frame size.

Each of the previously described IR systems measures the IR emission over a single wavelength or color band, typically 8-12 μm. Unfortunately single color systems are sensitive to the tile emissivity, which changes strongly with lithium deposition. While graphite has relatively low optical reflectivity at infrared (IR) wavelengths ($R<0.15$), liquid Li is highly reflective ($R>0.9$). High reflectivity, combined with variable emissivity of Li as fuel and impurities are absorbed, greatly complicates critical interpretation of infrared photon flux from plasma-facing surfaces in NSTX which, near the divertor, may be subject to temperatures of $>1,000$ °C and heat fluxes of >10 MW/m^2. This high heat flux makes the capability to diagnose surface conditions using IR with sufficient temporal and spatial resolution essential for successful operation of the LLD.

We note that past NSTX heat flux data were obtained before lithium coatings were used in any given calendar year. In 2010, the NSTX IR system was modified[27] to simultaneously view two wavelength bands or 'colors'. A schematic of the optical layout is given in figure N2-1.
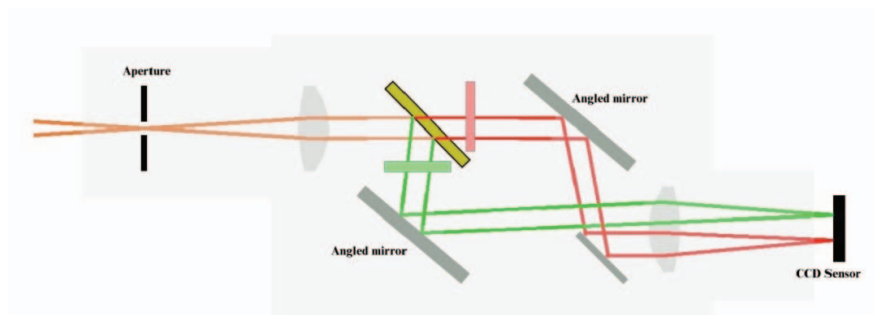

*Figure N2-1: Optical layout of the Cairn Optosplit II image splitter*

The beam-splitter divides the IR image into two beams using a custom IR dichroic beamsplitter, through separate bandpass filters, and then re-projects the two images side-by-side onto the existing camera detector. By assuming that the emissivity is the same in these two color ranges, the ratio of the signals becomes insensitive to emissivity; this is the basic premise of pyrometers. This upgrade allows for an assessment of the impact of lithium on the SOL heat flux width, as well as general measurements during lithium operation. Figure N2-2 shows the camera and splitter installed on NSTX.
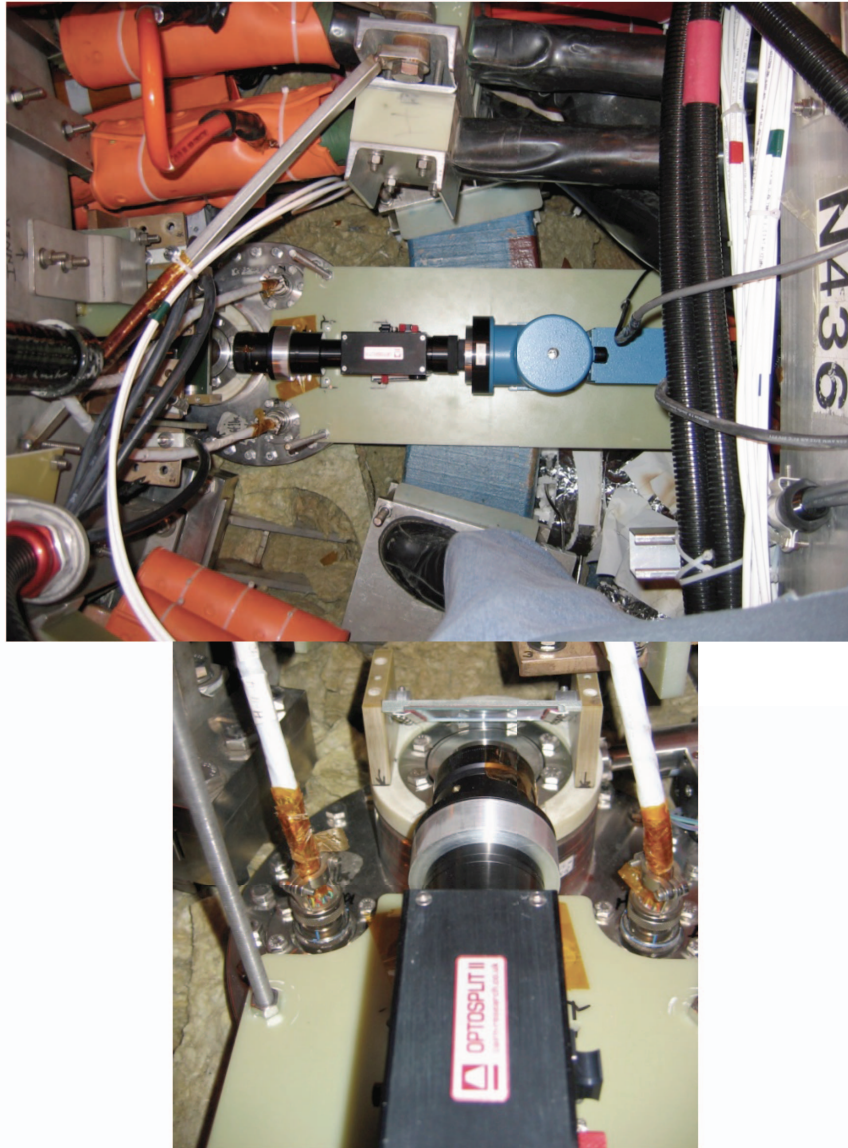
Figure N2-2: Camera layout on NSTX, including the custom designed optical splitter, which is positioned between the camera and the mirror.

The key enabling technology for the dual-band imaging adapter is a long-wave pass dichroic beamsplitter which efficiently separates MWIR and LWIR photons. For this project, Lambda Research Optics developed a dichroic which, when mounted at 45° to the impinging optical path, transmits the 7 – 10 μm (LWIR) spectral band with $T_{avg}\sim92\%$ efficiency, and reflects the 4 – 6 μm (MWIR) spectral band with $R_{avg}\sim99\%$ efficiency. The splitting technique effectively divides the available pixels in one of the two directions by 2, since the images are displayed side-by-side. Thus either a wider toroidal view or radial view of the liquid lithium divertor (LLD)[28] is possible, as shown in Figure N2-3. Here, the reported heat flux results used the radial view.
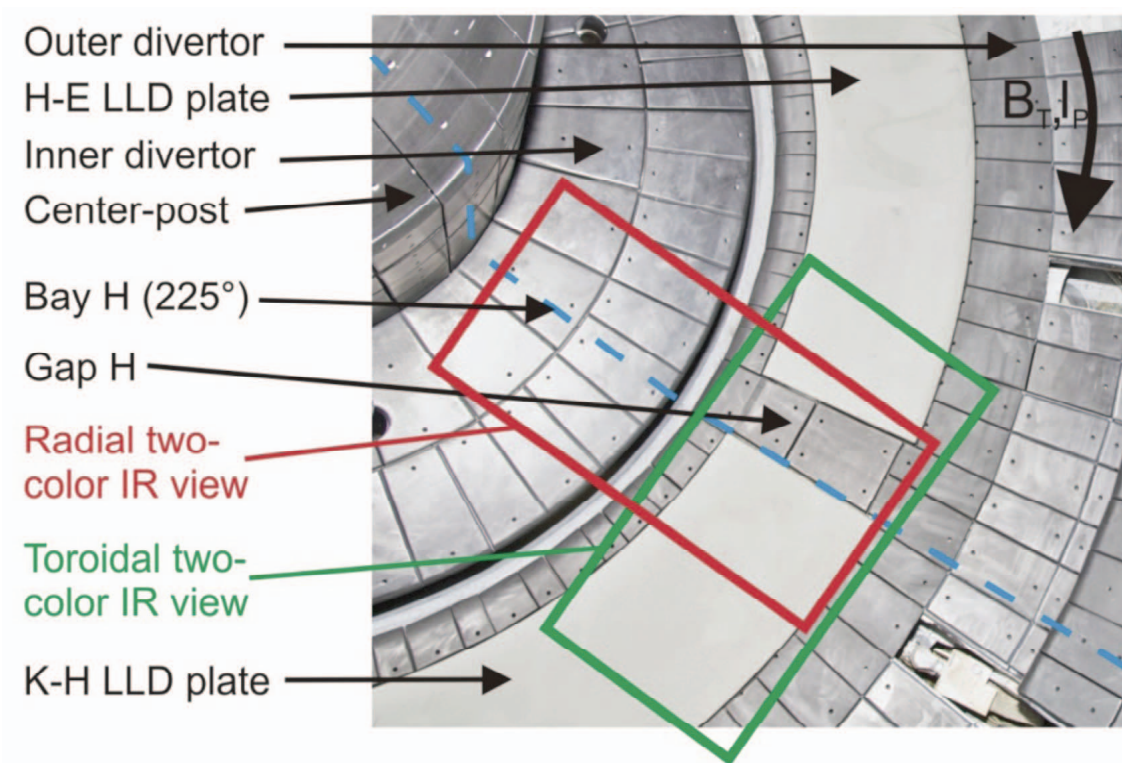
Figure N2-3: Plan view showing possible IR camera views because of the 2-color splitting technique, that effectively reduces the pixels per view to about 60 x 120. The heat flux data presented in this report are from the radial view.

The two-color system was put through an extensive set of bench calibrations, as well as in-situ calibrations. Figure N2-4 shows that the ratio of the intensities in the two colors from a bench calibration. The ratio of the intensities of the long wavelength (7-10μm) IR to the mid-wavelength (4-6μm) IR is a quantifiable function of temperature, with good sensitivity between 50~500ºC, proving the validity of the two-color technique for this

application. A recent refinement has expanded the sensitivity of the two-color system up the range 30~800ºC, which is sufficient for most NSTX discharges between ELMs and during smaller ELMs. We are now determining if cross-calibration between the individual long and mid-wavelength data with the two-color ratios can provide the surface temperature and heat flux during the larger ELMs.
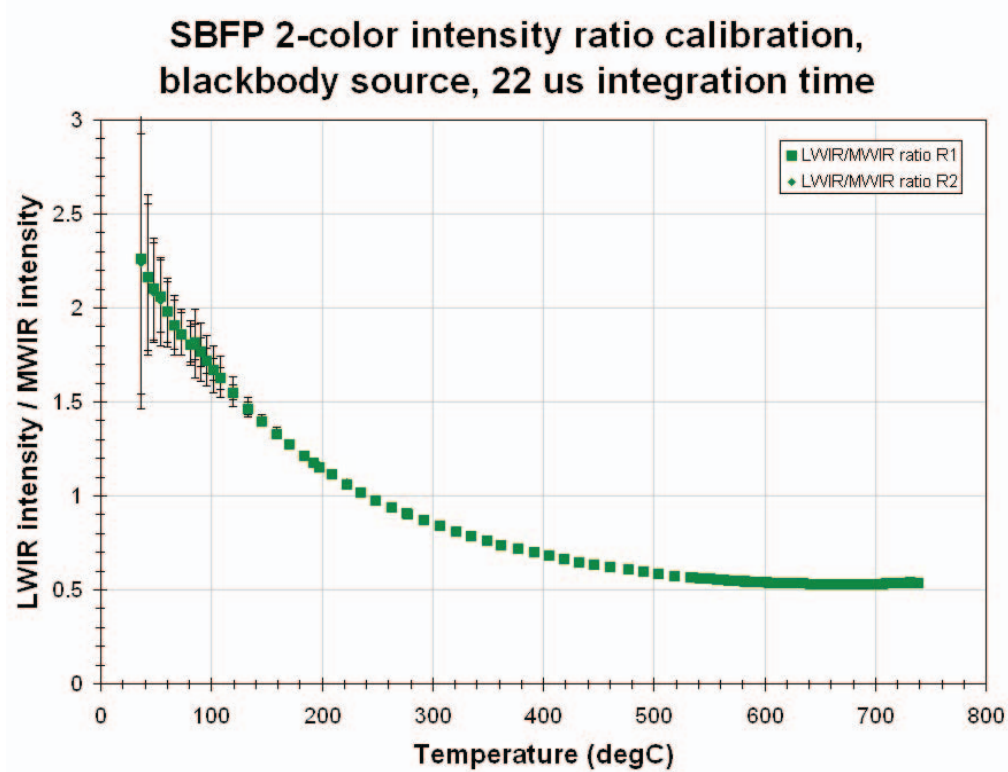

Figure N2-4. Ratio of the 2-band IR intensities (I_{LWIR}/I_{MWIR}) of the NSTX 2-color IR camera system as a function of the temperature during a black body source calibration. Here LW=long wavelength, and MW=mid-wavelength.
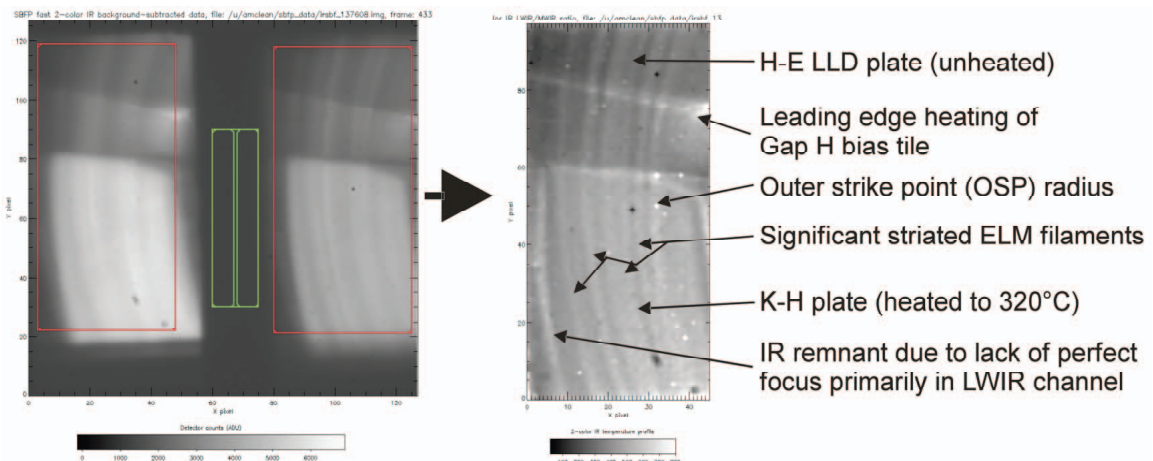

Figure N2-5: Example of the side-by-side projection using the beam splitter. The two color technique actually enhances contrast to LLD heating by ELM filaments. Note the IR remnant near the left edge of the analyzed image, which is not related to filamentary heating.

9

An example of the temperature data obtained from the two-color technique for the toroidal view is shown in Figure N2-5. As a point of interest, the two-color technique seems to enhance filamentary heating from ELM filaments. In much of the data from 2010, the plasma was operated in an ELM-free mode, because of the tendency of lithium to reduce the density profile and suppress ELMs[29-32]. In ELM-free discharges, there is no sign of filaments in the two-color data, demonstrating that the filament images are not an artifact of this technique.

The advantages of two-color technique are especially evident when the lithium in the LLD goes through a phase change[27]. Figure N2-6 shows the data from a discharge in which the LLD temperature remained at the freezing temperature, 180 °C, at the end of a discharge, as measured by thermocouples in the LLD. The two-color data showed the LLD temperature indeed stayed at the freezing point, but the single color data falsely indicated a decaying lithium temperature, likely because of the change in lithium emissivity across the freezing point.
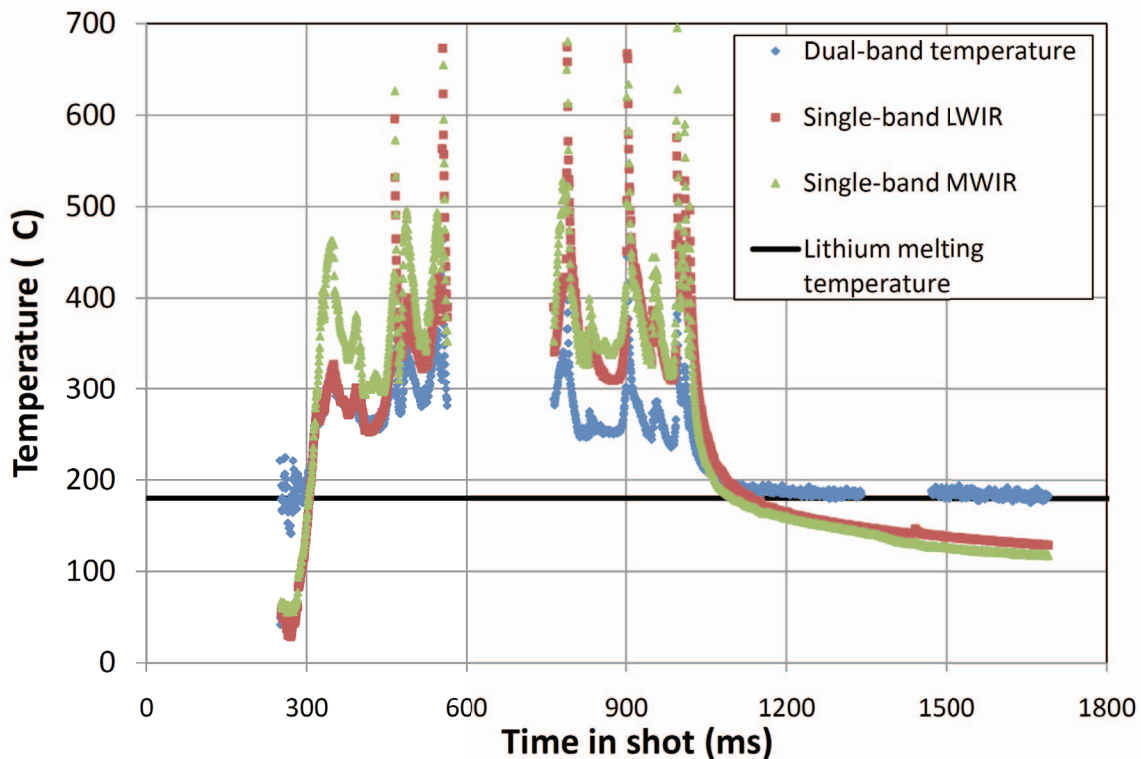

Figure N2-6: Comparison of two-color temperature and those obtained from the individual colors for a discharge where the lithium is passing through the freezing point at 180 °C at the end of the discharge at ~ 1.1 sec. The rapid peaks are due to a few ELMs and magnetohydrodynamic activity at the end of the discharge.

N3. Heat flux width dependences in discharges without lithium conditioning

Substantial effort was given to detailed analysis[18, 33] of the heat flux widths from existing NSTX datasets[10, 34-37] that were focused on heat flux scaling experiments in H-
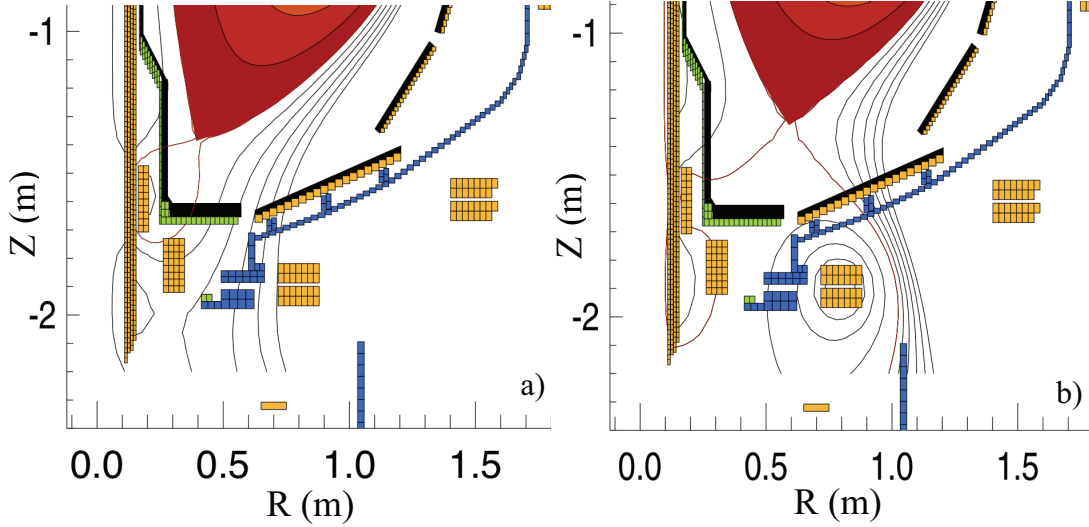

Figure N3-1: EFIT equilibrium reconstructions for 2 discharges with different plasma shapes. (a) High δ discharge (shot# 128640, 0.4 s) with δ ~ 0.7, κ = 2.3 and f_{exp} = 16. (b) Low δ discharge (shot# 132341, 0.41 s) with δ ~ 0.44, κ = 2.1 and f_{exp} = 4.

mode. These datasets were all obtained without lithium wall conditioning; the operating scenario used periodic boronizations along with helium glow discharge cleaning between discharges. Nearly all of the discharges had small, Type V ELMs, and some of these also had large Type I ELMs. The temperatures were measured with an IR camera[24] operated at 30 Hz, and the heat flux was computed from a 1-D semi-infinite conduction model. The data from these existing datasets were obtained in a variety of shapes, including both low δ and high δ, e.g. are shown in Figure N3-1.

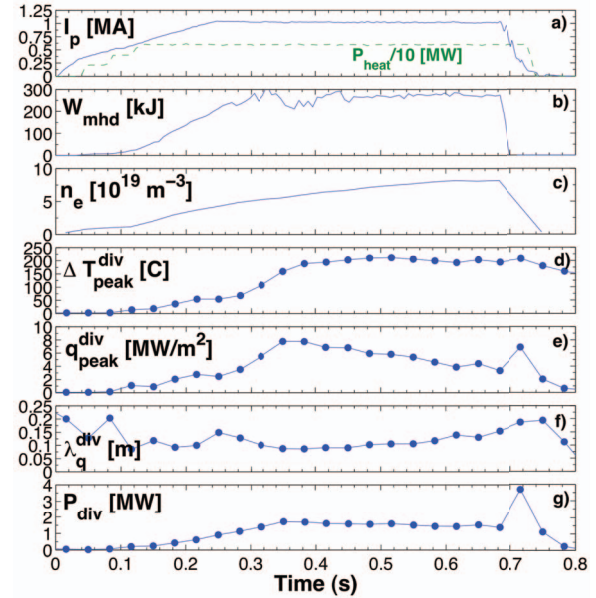*Figure N3-2: Typical progression of discharge parameters for NSTX (#128640) in a) I_p and P_{heat}, b) plasma stored energy, W_{MHD}, c) $\overline{n}_e$, d) ΔT_{peak}^{div} e) q_{div}^{peak}, f) λ_q^{div} and g) power to the outer divertor, P_{div}. To appear in T.K. Gray et al, J. Nucl. Mater. (2011) at press.*

11

It should be noted that the heat flux profile does not stay constant during the evolution of NSTX discharges, which typically have a secular density ramp. Figure N3-2 shows a typical evolution of discharge parameters. Note in particular that the peak surface temperature rise, ΔT_{peak}^{div}, flattens out, and that the peak divertor heat flux, q_{peak}^{div}, usually rolls over as the density increases, mostly due to a broadening of λ_q^{div}. The power incident on the outer divertor remains roughly constant. Thus, for the analysis presented here, we typically analyze a 100-150ms period of peak heat fluxes, which
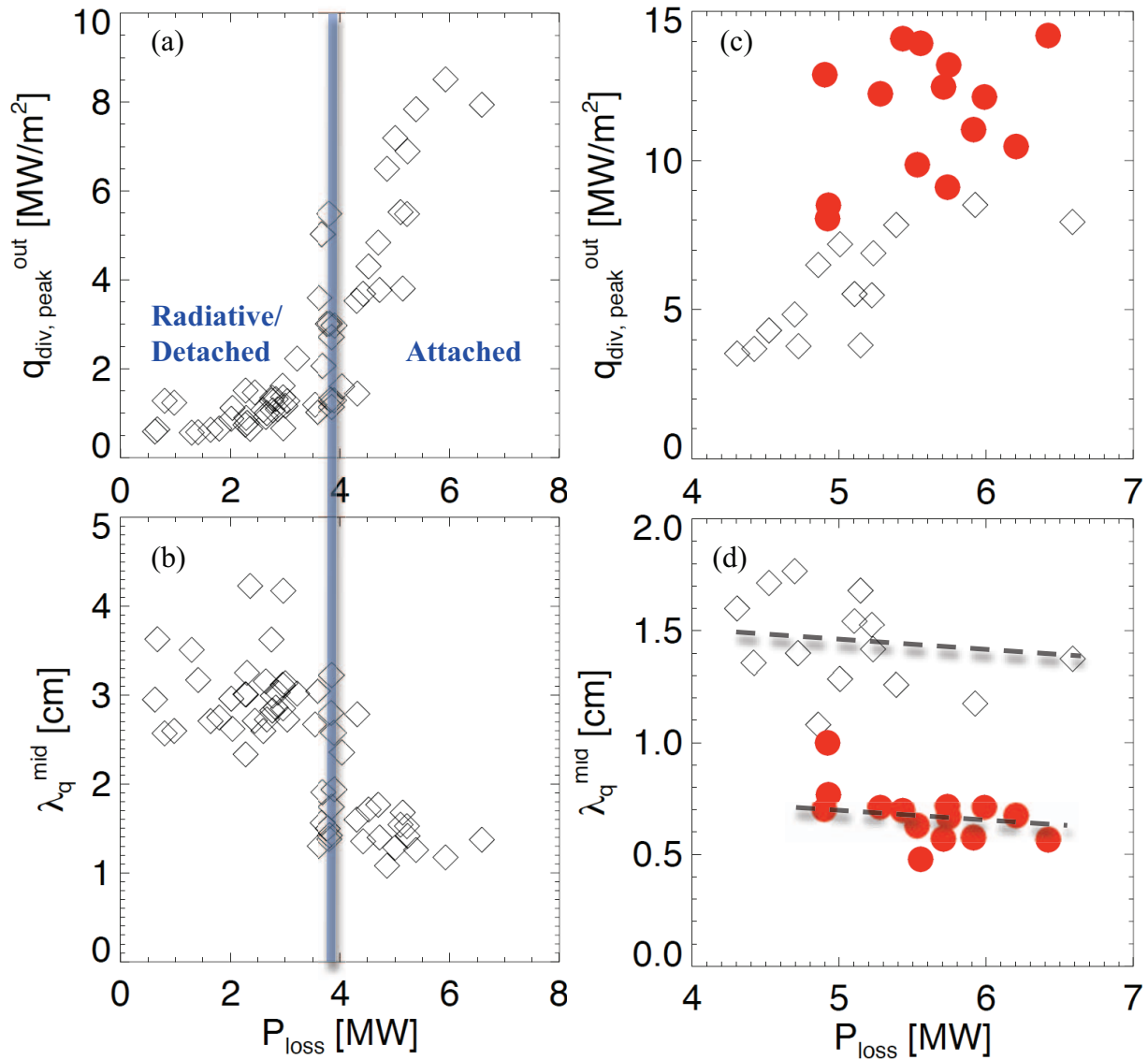

Fig. N3-3: *dependence of peak outer divertor heat flux and midplane-equivalent widths on power flow into the SOL, P_{loss}. The black diamonds were obtained at intermediate triangularity $\delta \sim 0.5$ and $I_p = 0.8$ MA, whereas the red circles were obtained at high $\delta \sim 0.7$ and $I_p = 1.2$ MA. To appear in T.K. Gray et al, J. Nucl. Mater. (2011) at press.*

corresponds to the lowest λ_q^{div}. This choice is made to provide a conservative estimate for projections, and it anticipates success in the density control program, which is aimed partly at eliminating the density ramp.

Previously we reported[10, 11] that the peak heat flux increased with power flowing into the SOL, P_{loss}. A refined analysis of those data shows that λ_q^{mid} is relatively independent of power flowing into the SOL when the divertor is in the "attached" state, i.e. with relatively low radiated power and momentum loss. Figure N3-3a,b illustrates these points from a set of discharges at intermediate $\delta=0.5$ and $I_p=0.8$ MA: at $P_{loss} \simeq 4$ MW, there is a clear transition to a narrow footprint in terms of λ_q^{mid}. For higher P_{loss}, the λ_q^{mid} appears insensitive with a range between 1.0-1.8 cm. Figure N3-3c, N3-3d plots the dependences over the P_{loss}, range 4-7 MW, with data from a sequence of high $\delta=0.7$ and $I_p=1.2$ MA discharges. The relative insensitivity of λ_q^{mid} to P_{loss} is apparent in that dataset also. On the other hand, the large difference between λ_q^{mid} for these two conditions points to an I_p (or an edge safety factor, q_{95}) dependence.

One of the main differences between the low and high I_p discharges above is the divertor flux expansion, which is much higher in the high I_p discharges. We therefore examined the dependence of λ_q^{mid} with f_{exp}. A wide scan in the divertor flux expansion was accomplished in past NSTX experiments[37] by variation of the X-point
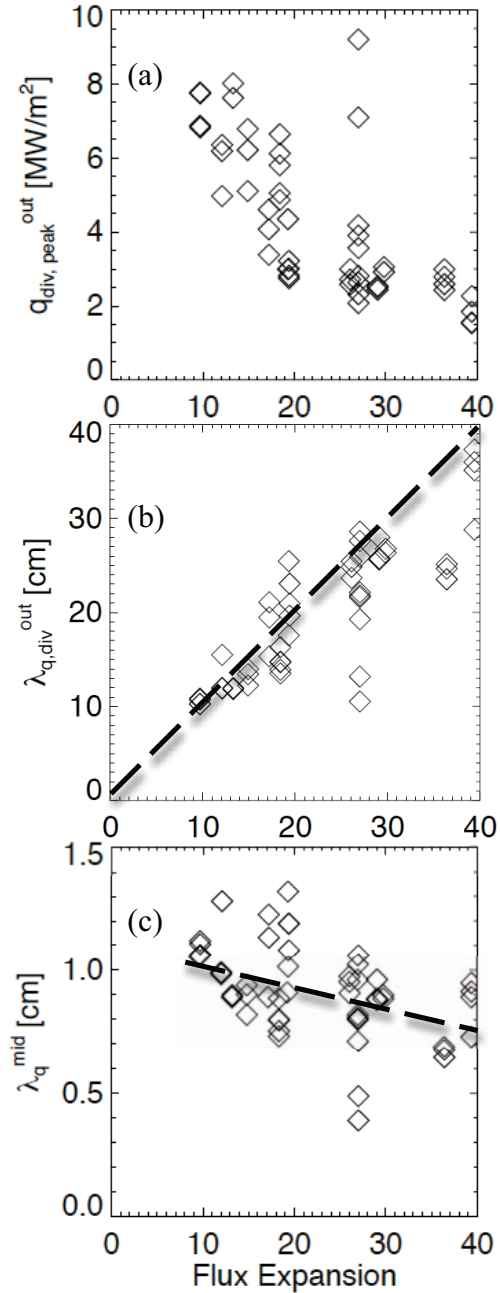

Fig. N3-4: dependence of (a) peak heat flux, (b) divertor heat flux width, (c)and (mapped) midplane heat flux widths on divertor magnetic flux expansion. To appear in T.K. Gray et al, J. Nucl. Mater. (2011) at press.

13

height[37]. The goal here is to evaluate the dependence of the divertor and midplane heat flux footprint widths on flux expansion. It was found that the $q_{div,peak}^{out}$ decreased inversely with flux expansion (Figure N3-4a), and that the total power incident on the outer divertor was approximately constant. Thus the outer divertor heat flux profile width, λ_q^{div}, scaled nearly linearly with flux expansion over a wide range (Figure N3-4b). Consequently, the λ_q^{mid} contracts only weakly on magnetic flux expansion, if at all (20% reduction over a factor of 4 change in flux expansion).

Using the results shown in the two preceding figures that the λ_q^{mid} is in relatively insensitive to P_{loss} (for high P_{loss}) and flux expansion, data from different δ and f_{exp} can be combined to quantify the dependence of $q_{div,peak}^{out}$ and λ_q^{mid} on I_p. This is shown in Figure N3-5. All of these discharges had a fixed B_t=0.45 T. Here the $\lambda_q^{mid} \sim I_p^{-1.6}$, i.e. faster than inversely with I_p, consistent with past results[10]; in comparison, DIII-D[9] and JET[38] have reported an $\lambda_q^{mid} \sim I_p^{-1}$ in the past. Part of the scatter in the NSTX data is related to the weak remnant dependence on P_{SOL} and f_{exp}, and partly due to slightly different fueling and divertor radiation regimes. Nonetheless the strong dependence of the SOL width on I_p is apparent, and therefore critical to understand in projection to higher future devices with higher I_p. One possibility of the underlying physics is a dependence on β_{pol}, which could originate from neoclassical transport considerations.

The data described in this section were shared between the three facilities. Looking ahead for NSTX-Upgrade, the prediction is for ~ a 3mm SOL width at I_p=2 MA, which will require very high flux expansion and/or partial detachment to handle for the 5 sec design pulse length.
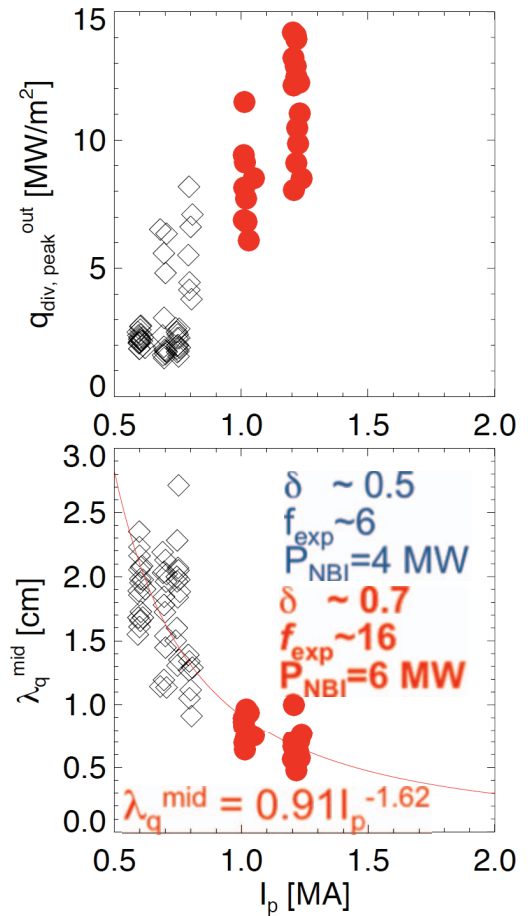

Fig. N3-5: dependence of peak outer divertor heat flux and midplane-widths on I_p. To appear in T.K. Gray et al, J. Nucl. Mater. (2011) at press.

14

N4. Heat flux width dependences in discharges with lithium coatings

Because all of the previous data were from discharges without lithium coatings, the focus of new experiments in 2010 was to measure the effect of lithium on SOL widths with the new two-color IR camera described in Section N2, in H-mode discharges. The biggest change due to the lithium was a transition from ELMy discharges (either Type V, Type I, or mixed Type I/V ELM regimes[39]) to ELM-free discharges. The new data included single-parameter scans in I_p, B_t, P_{NBI}, δ_r^{sep}, and measurements of the heat flux profile in a poloidal cross-section shape that matches a scaled C-Mod and DIII-D shape used in small ELM similarity studies[19, 20]. Much of the data were obtained with a 'high' lithium evaporation rate of 300 mg per discharge, which tended to make the plasmas nearly completely ELM-free. Additional data were obtained with a 'medium' lithium evaporation rate of 150 mg per discharge, which tended to make the plasmas somewhat more prone to ELMs. All of the data analysis presented here was done with the 1-D semi-infinite slab conduction model mentioned above; however, the fast IR camera appears to be more sensitive to surface film effects (e.g. poor thermal contact) because of the fast framing speed. Hence,
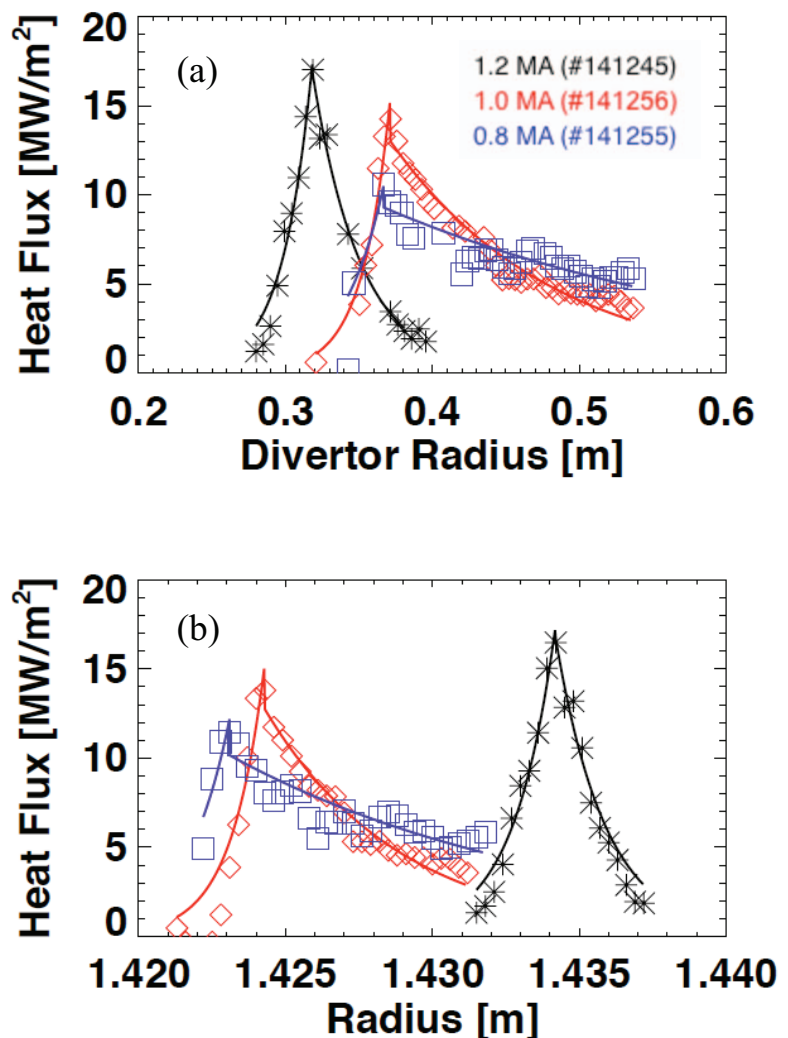

Figure N4-1: Dependence of (a) divertor and (b) midplane mapped heat flux profiles for three different I_p, demonstrating that the λ_q^{mid} also contracts with I_p in ELM-free discharges with lithium wall coatings.

the intensity calibrations and computed heat fluxes could be 100%-200% high, and those data should be considered preliminary, pending the application of a 2-D calculation with the THEODOR code[40]. The heat flux widths should be more reliable. In this section, the data from the 'medium' evaporation rate endpoints are shown, to illustrate the trends. All data are obtained between ELMs, if present, and averaged over 6-12 msec.

A fine I_p scan was obtained from 0.7 to 1.3 MA in 0.1 MA increments; the other discharge parameters were P_{NBI}=3 & 4 MW, B_t=0.45 T, $\delta_r^{sep} \sim$ -5mm, and elongation κ ~2.4. Figure N4-1 compares the measured divertor profiles for 0.8, 1.0, and 1.2 MA, as well as the profiles mapped to the midplane. The trend presented in the previous section that λ_q^{mid} drops faster than inversely with I_p in ELMy discharges is evident in these ELM-free discharges also.

A fine B_t scan was also obtained from 0.33 to 0.55 T, in increments of 0.025-0.05 T. The other discharge parameters were P_{NBI}=4 MW, I_p=0.8 MA, $\delta_r^{sep} \sim$ -5mm, and elongation κ ~2.4. Figure N4-2 compares the heat flux profiles from two different B_t values: there is no discernible impact of the B_t magnitude on
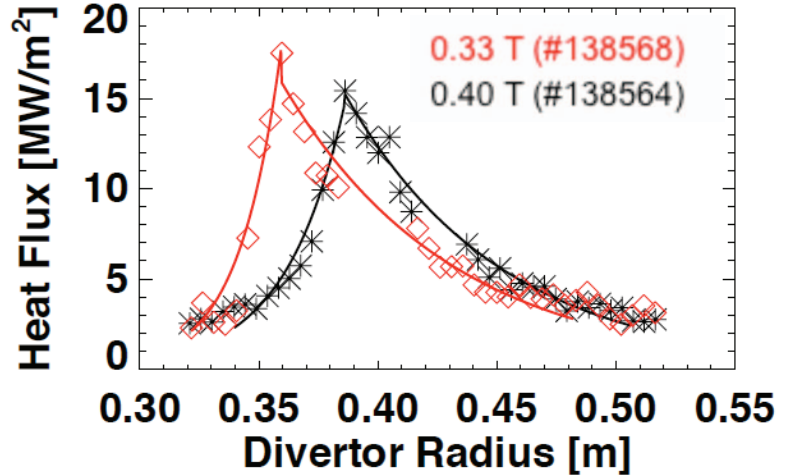

Figure N4-2: Dependence of divertor heat flux profiles for two different B_t, indicating that the λ_q^{mid} is independent of B_t in ELM-free discharges with lithium wall coatings.
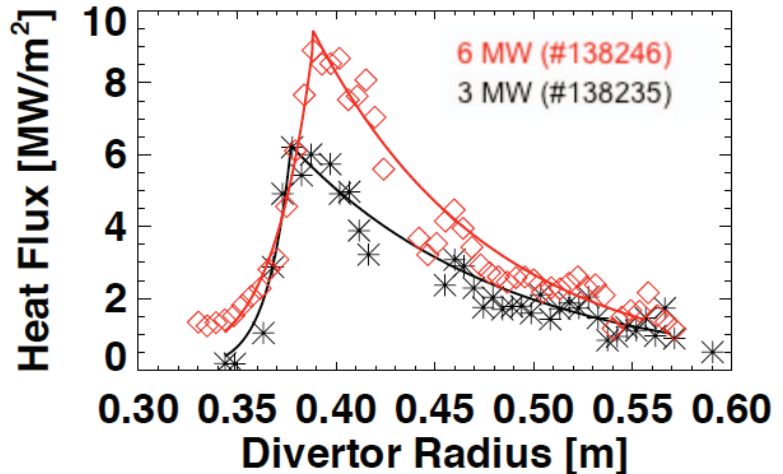

Figure N4-3: Dependence of divertor heat flux profiles for two different P_{NBI}, indicating that the λ_q^{mid} is largely independent of P_{NBI} in ELM-free discharges with lithium wall coatings.

16

the heat flux profile. From this, we conclude that the observed I_p dependence is not a q_{95} dependence. Clearly the higher $B_t \geq 0.5$ T data will help clarify this, once the pending analysis is completed.

A P_{NBI} scan from 2 MW to 6 MW in 1 MW increments was obtained at both 0.8 MA and 1.2 MA. As expected the peak heat flux goes up with P_{NBI}, but λ_q^{mid} is still relatively insensitive to P_{NBI}, as shown in Figure N4-3 and as seen in the ELMy discharges without lithium. It is a bit surprising that the peak heat flux did not increase linearly with input power as normally observed – additional time slices are being analyzed to determine if this is a reproducible effect.

A detailed δ_r^{sep} scan was obtained, starting from balanced double-null configuration with $\delta_r^{sep} \sim 0$ mm to strongly lower-single null with $\delta_r^{sep} \sim$ -20 mm, in ~2.5 mm increments. The standard convention is used that $\delta_r^{sep} < 0$ means the lower divertor is dominant; the ion grad-B drift is toward the lower divertor, here and in all the presented NTSX data. The lower divertor peak heat flux increased with decreasing δ_r^{sep} (Figure N4-4), qualitatively consistent with the single-null/double-null comparison done previously[41] in NSTX. At the two smaller δ_r^{sep} values, the heat flux widths were
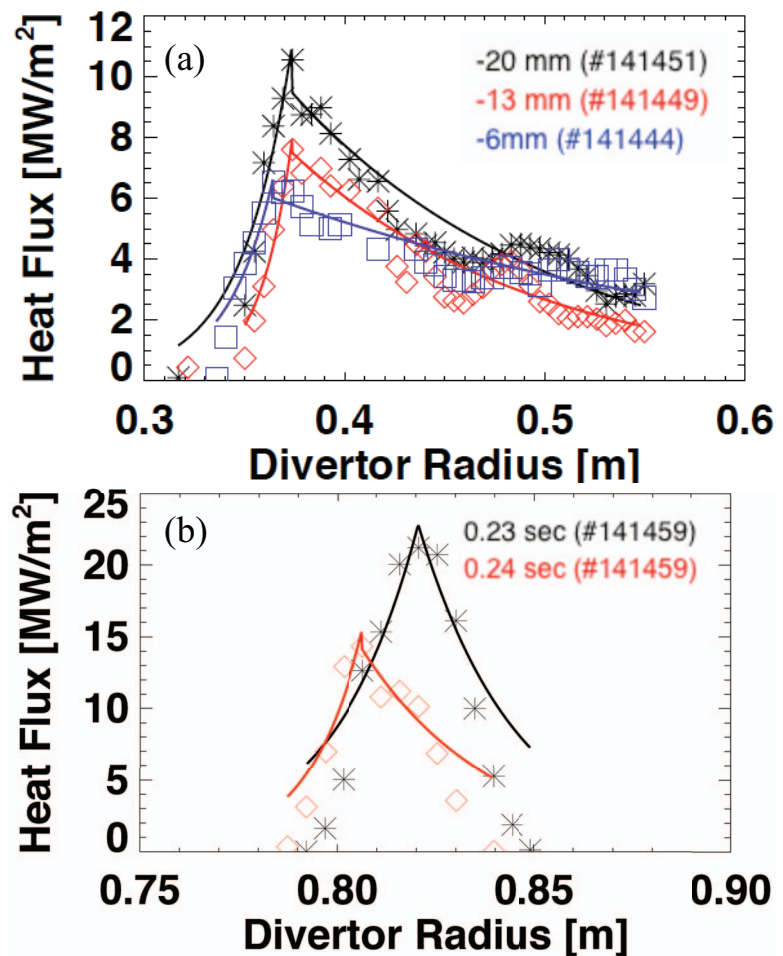

Figure N4-4: Dependence of divertor heat flux profiles for (a) three different δ_r^{sep} values, and (b) two time slices in a low δ, low f_{exp} boundary shape that matched C-Mod and DIII-D.

similar, while the profile was broadened at the largest δ_r^{sep} closest to double-null. Analysis of the entire dataset is in progress.

Finally a set of low δ, low f_{exp} discharges were run to match a scaled poloidal cross-sectional shape from Alcator C-Mod and DIII-D, previously used for small ELM similarity studies. Figure N4-4b shows that the divertor heat flux profiles are very narrow because of the low f_{exp}. Indeed profiles look more Gaussian than exponential, hence the poor match between the fits (used only to guide the eye) and the data. The λ_q^{mid} values for these discharges $\sim$ 12 mm, consistent with the low I_p, low δ data presented from the ELMy discharges in section N3.

In summary, the new data obtained in FY 2010 with lithium wall coatings qualitatively supports the dependences from existing older data sets, namely that the λ_q^{mid} decreases strongly with I_p, and is largely independent of P_{loss}. In addition the new data confirms that the magnitude of B_t does not affect λ_q^{mid}, indicating that the observed I_p dependence is not related to q95 or connection length. Also, we have obtained new data showing that λ_q^{mid} is independent of δ_r^{sep} for δ_r^{sep} < -10 mm; analysis is in progress to see if the observed broadening of λ_q^{mid} near double null as δ_r^{sep} approaches 0 is a general trend. Finally our peliminary indications are that lithium coatings/ELM-free discharges do indeed reduce λ_q^{mid} (not shown here), but additional analysis is required to quantify this.

We close with a caution that the data analysis presented in this section should be considered as preliminary. In particular the magnitudes of the heat fluxes are probably too high, but the widths should be ok.

N5. Associated heat flux profile studies

a. Snowflake divertor studies

Analysis of divertor characteristics with an innovative divertor configuration, i.e. the "snowflake divertor" (SFD)[21], represents part of NSTX's contribution to this milestone from the perspective of improved heat flux handling. This magnetic topology was recently realized in NSTX[22, 23, 42], resulting in divertor peak heat flux reduction and impurity control. In this case, the divertor heat flux footprint is broadened by easing the access to partial detachment, which leads to a substantial increase in the midplane-equivalent footprint.

In preliminary NSTX experiments with the SFD configuration, a reduction in peak divertor heat flux due to a partially detached strike point region, and a significant reduction in core carbon density and radiated power were observed, in 0.8 MA 4-6 MW NBI-heated H-mode discharges. These initial experiments confirmed the attractive SFD properties predicted by analytic theory[21] and two-dimensional multi-fluid numerical modeling[43]. The SFD concept uses a second-order X-point created by merging, or bringing close to each other, two first-order X-points of a standard divertor configuration. The possibility of forming the SFD configuration has been demonstrated through magnetic equilibria modeling for DIII-D and NSTX, and in experiments on TCV[44]. The SFD-like configuration was generated in NSTX
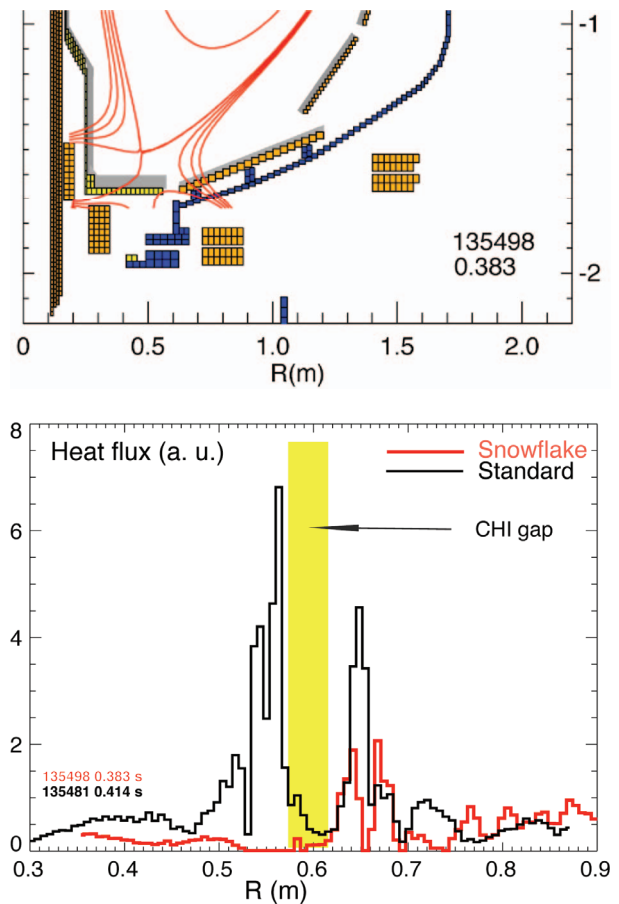

Fig. N5-1. (Top) The "snowflake" divertor configuration obtained in NSTX with 3 mm SOL flux surfaces shown; (bottom) Divertor heat flux profiles measured by IR camera in discharges with a standard medium δ divertor and with the "snowflake" divertor configurations [V.A. Soukhanovskii, et al., Phys. Rev. Lett. (2010) submitted].

using two divertor magnetic coils controlled in real time by the plasma control system, e.g. Figure N5-1. When compared to the high-triangularity (δ=0.7-0.8) standard divertor configuration in NSTX[36], the obtained SFD configuration with a medium triangularity (δ=0.5-0.65) had a connection length $l_{\parallel}$ longer by factors of 1.5-2, and a divertor poloidal flux expansion f_{exp} higher by factors of 2-3. Divertor heat flux profiles showed low relative heat flux in the greatly expanded region near the outer divertor strike point during the SFD periods (Fig. N5-1); not that the inner strike point is not shown in either heat flux profile; the yellow shading is for a tile-free gap, from which there is no IR emission.

Divertor radiation due to carbon impurity was significantly increased in the SFD. As inferred from the spatially-resolved ultraviolet spectroscopy measurements and collisional-radiative and Stark spectral line broadening modeling, a volume recombination region with $T_e \sim$ 1.5 eV, $n_e > 3 \times 10^{20}$ m^{-3} developed in the X-point and strike point regions, suggesting an increase in volumetric momentum losses in the divertor and a partial detachment of the first several mm of the SOL width, as mapped to the midplane. Importantly, the SFD partial detachment was obtained in reduced density discharges with lithium conditioning, in contrast to previous NSTX divertor detachment experiments that
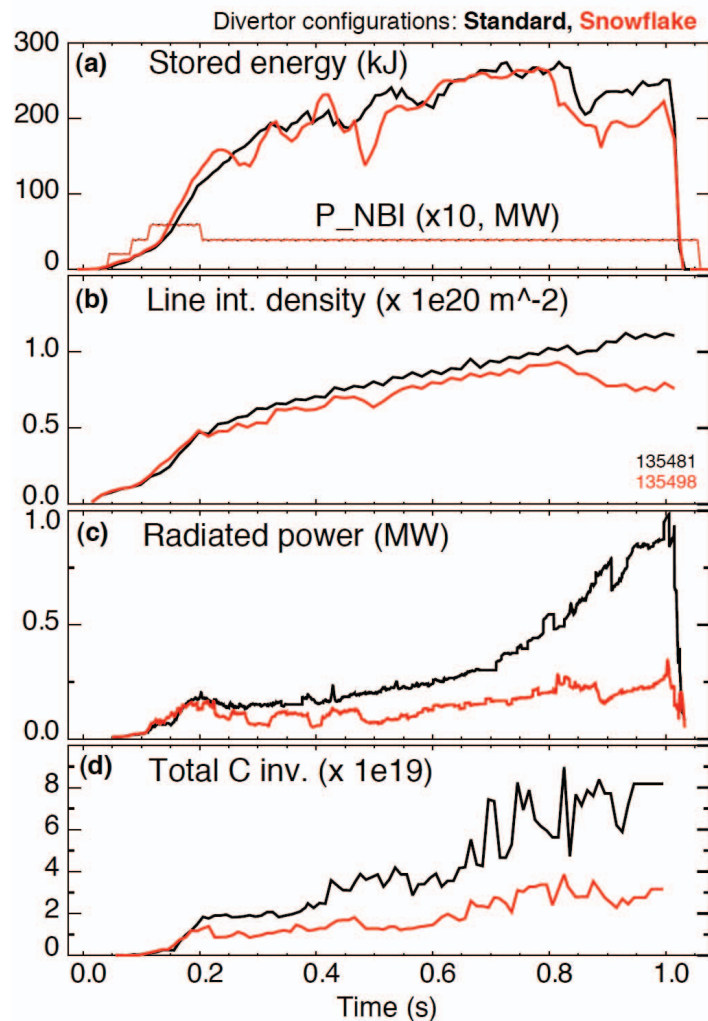

Figure N5-2: Time histories of core and edge plasma quantities of the standard divertor and snowflake divertor discharges: (a) Stored energy W_{MHD} and P_{NBI} ; (b)line integrated electron density; (c) Core radiated power P_{rad}; (d) Core carbon inventory [V.A. Soukhanovskii, et al., Phys. Rev. Lett. (2010) submitted].

required an additional divertor gas injection[36].

The core carbon density and core radiated power were reduced by up to 50 % in the SFD discharges, with no degradation of H-mode stored energy and confinement (Figure N5-2). The reduction in carbon density resulted also in a reduction of the line-average density. These good results were obtained in early experiments that achieved the SFD configuration transiently for 50-100ms periods; when added together, these periods represent about 50% of the flattop duration.
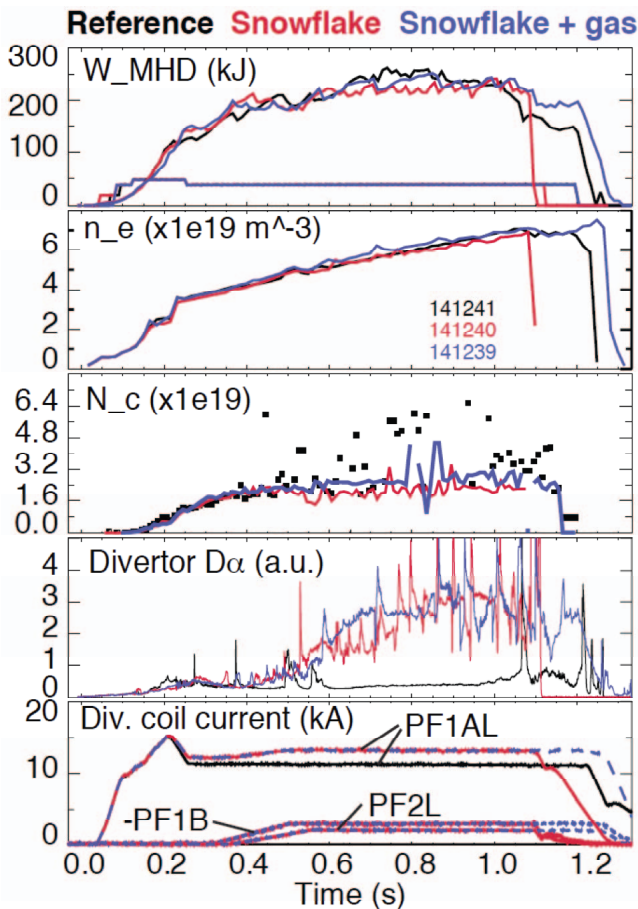

Figure N5-3: Time histories of the standard (reference) divertor, snowflake divertor, and snowflake divertor with divertor gas puffing discharges: (a) Stored energy W_{MHD}, (b) line-averagr density from Thomson, (c) Core carbon inventory, (d) Divertor D_α emission, and (e) Divertor coil currents used to make the SFD. The inset in panel (a) is the common P_{NBI} waveform.

The preliminary experiments with the SFD were followed by additional feedback control development, resulting in SFD configurations for the majority of the discharge pulse length. Figure N5-3 compares three discharges: a reference high δ discharge, a discharge with the SFD, and a discharge with the SFD and additional divertor gas puffing, all at 0.9 MA, 0.45 T, and 4 MW NBI. Panel N5-3d shows that the reference discharge used only the Pf1al coil. The SFD phase was initiated by use of the Pf1b coil, followed by the Pf2l coil, which were ramped sequentially from 0.3-0.5 sec. Panel N5-3d shows that the divertor D_α was substantially and steadily higher in the SFD discharges, which is symptomatic of the partial detachment and volume recombination facilitated with the configuration. The core carbon inventory is maintained at a steady level with the SFD, whereas it gradually increased in

the reference discharge. The stored energy was largely unaffected in the SFD configuration.

Interestingly both of the SFD discharges had ELMs as seen in panel N5-3d, whereas the reference discharge was ELM-free. This makes comparison of the core impurity content difficult, since ELMs are known to flush impurities, i.e. the reduction may not be attributable to the SFD alone in this set of discharges. On the other hand, the periodic heat pulses due to the ELMs provide useful time markers in comparison of the heat flux profiles. Figure N5-4c-e shows that the SFD effectively reduced the peak heat flux between ELMs, but the peak heat flux during the ELMs is still observed, suggesting transient re-attachment between ELMs. Panels N5-4f,g compare the heat flux profiles between ELMs for these three discharges at two different times, demonstrating substantial reduction between the reference and SFD discharges. Thus, the SFD
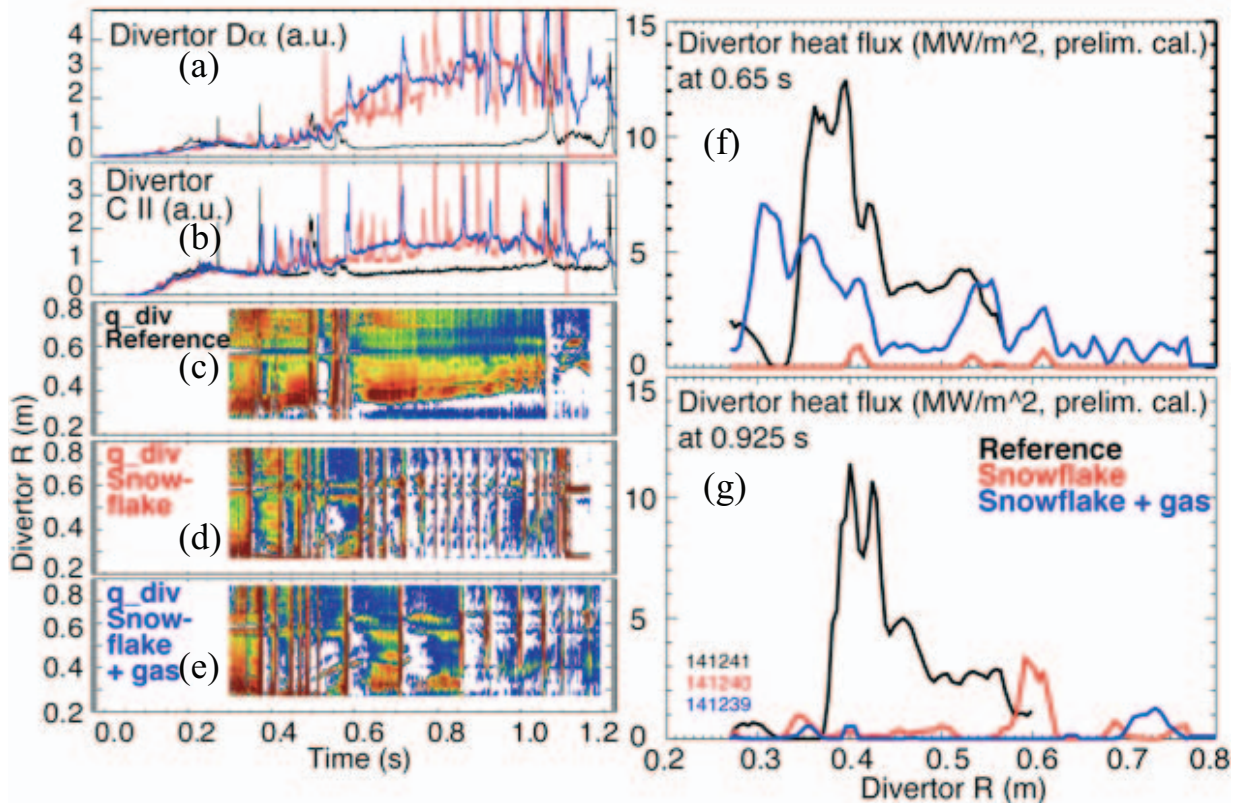

Figure N5-4: Time histories of the standard (reference) divertor, snowflake divertor, and snowflake divertor with divertor gas puffing discharges: (a) Divertor D$_\alpha$ emission, (b) Divertor C–II emission, (c) contour plot of heat flux from fast IR from reference, (d) contour plot of heat flux from fast IR from SFD, (e) contour plot of heat flux from fast IR from SFD plus gas puffing, (f) radial heat flux profile comparison at 0.65 sec, and (g) radial heat flux profile comparison at 0.925 sec.

22

configuration is a very promising method to reduce the peak heat flux in existing devices. The simplicity of the SFD, i.e. use of only two divertor coils, should be extrapolable to future devices, thereby partly offsetting the anticipated contraction at higher I_p.

N5b. Effect of 3-D fields on profiles

The application of small, 3-D magnetic field perturbations produced by internal or external coils has been found to have significant impact on the plasma performance in tokamaks, i.e. error field and resistive wall mode control[45], ELM suppression[46] and ELM triggering[47]. At the present time, ITER is considering the use of non-axisymmetric magnetic perturbation for the ELM control; thus, the effect of these intrinsic and imposed 3-D fields on the heat and particle footprints on the divertor plates is of substantial interest.

When external 3-D fields are applied, the modification of the magnetic equilibrium produces a 3-D structure of perturbed magnetic field lines in the plasma edge, where the poloidal magnetic flux is re-organized into topological structures known as homoclinic tangles[48]. The perturbed separatrix is split into multiple invariant manifolds, forming a 3-D "lobe" structure connecting to the open field lines, which are a mixture of long connection length stochastic field lines and short connection length laminar field lines. The lobe structure of the open field lines generates a striated strike point pattern radially across the divertor target surface. This imposed magnetic field structure should be reflected in the measured divertor heat and particle flux profiles, due to the rapid parallel transport along the open field lines. Indeed, such an observation application was recently reported[49, 50] in DIII-D H-mode discharges during the application of Resonant Magnetic Perturbations (RMP). Specifically striated strike point patterns for heat flux were observed in high (>0.5) pedestal electron collisionality discharges, while particle flux showed striation was observed for both high and low collisionalities.

In NSTX, striations in the heat and particle flux profiles were observed with the application of 3D fields[51-53]. Here we summarize those results.

Figure N5-5 shows the poloidal cross section of NSTX showing the location of the fast IR camera[26, 54] and D_α camera diagnostic views, as well as the radial location of one of the six midplane window-frame external 3-D field coil. The magnetic equilibrium for a typical discharge is also overlaid. Also shown in figure N5-5 is the contour plot of the calculated connection lengths at the divertor surface using a vacuum field line following code with the application of external n=3 fields. The formation of the 3-D lobe structure

can be clearly observed. The D_α emission at the lower divertor target is measured by a 1-D CCD camera[55] installed at toroidal angle $\varphi=255°$. This camera was operated at 2kHz rate, with sub-mm spatial resolution, and is a part of the system of CCD arrays that are spectrally filtered for deuterium Balmer-α (656.1nm), Balmer-γ (433.9nm), and/or HeII Paschen-α (468.5nm) emission lines using $\Delta\lambda=1.0$-1.5nm bandpass interference filters[55]. It is known that the D_α emission is closely correlated with the particle flux in attached plasmas, due to its strong dependence on the plasma density; hence, we use D_α and particle flux interchangeably in this section, noting that one can be converted to the other by use of appropriate S/XB coefficients.
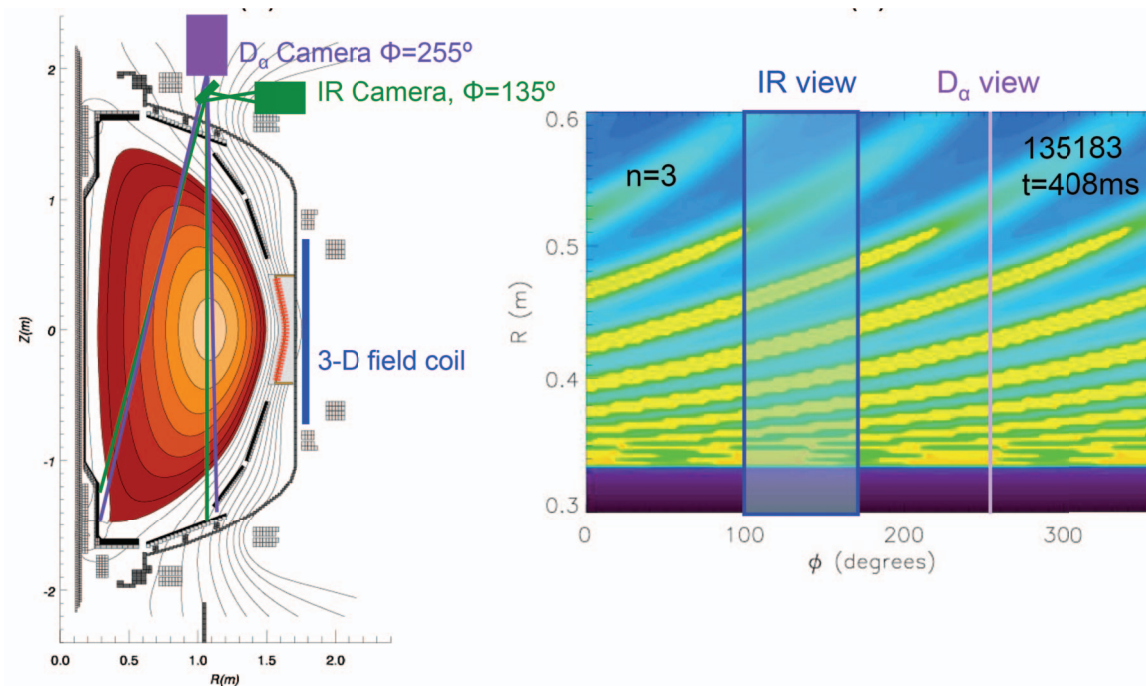

Figure N5-5: (a) Schematic of NSTX cross-section, showing views of the 2D IR camera and the 1-D D_α cameras, with the location of the external 3D field coil overlaid; (b) shows the contour plot of calculated connection lengths for n = 3 application, showing the formation of the lobe structure as a function of toroidal angle (φ) and radius. The radial and toroidal coverage of the D_α and IR cameras is also shown [J-W. Ahn, et. al., Nucl. Fusion 50 (2010) 045010].

Figure N5-6 compares the lower divertor IR images before and after the application of n=3 3-D field perturbation at t=400ms, along with the heat flux and D_α profiles. The data along row (a) show that there is negligible strike point splitting at an early stage of the discharge (t=180ms).

In this set of discharges, weak striations become apparent in the IR image before the external magnetic perturbation (t=0.398 sec, figure N5-6b). Both the heat flux and D_α profiles significantly broadened compared to those in figure N5-6b with modest local peaks in the profile. These multiple peaks and valleys are characteristic of the lobe structure shown in figure N5-5b. We hypothesize that these striations are due to intrinsic error fields, which produce observable strike point splitting. In fact, this 'intrinsic' strike point splitting starts to appear even earlier in the discharge, at t~0.2 sec, and is present in the remainder of the discharge. Note that intrinsic strike point splitting is not ubiquitous in NSTX; low δ discharges rarely see such splitting. The possible source of intrinsic error fields and the plasma conditions for the intrinsic splitting to occur are presently under detailed investigation.

The application of the 3-D fields augments this intrinsic splitting, making the striations brighter and clearer (t=0.432 sec, figure N5-6c). As the plasma evolves, the striations become more pronounced (t=0.482 sec, figure N5-6d). The widths of the heat flux and D_α profiles do not change significantly by the 'augmented' strike point splitting caused by the 3-D field application. Note also that the peak heat and particle flux values are largely unchanged during the 3-D field application.

Note that the enhancement of the striations can be as fast as 3-4 msec after 3D field application. This is consistent
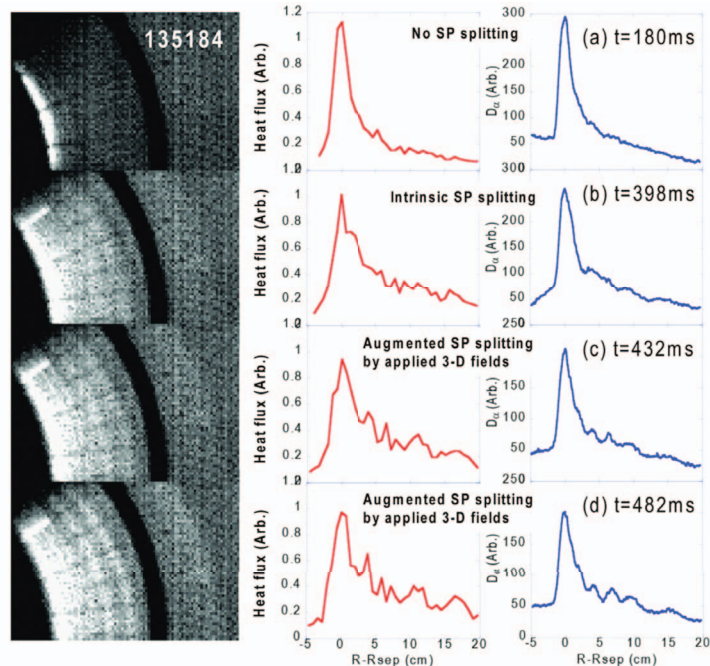

Figure N5-6: Unprocessed images of the IR emission across the lower divertor from the top of NSTX (left column); measured heat flux profiles (middle column), and D_α profiles (right column) from several time slices for a discharge with n = 3 fields applied at t = 0.4 sec. (Row a) no strike point (SP) splitting early in discharge, (b) 'intrinsic' profile splitting 2 msec before the 3D field application and (c), (d) 'augmented' profile splitting due to the applied 3D fields [J-W. Ahn, et. al., Nucl. Fusion 50 (2010) 045010].

with the measured time for a noticeable perturbation to develop through the vessel and the passive stabilizing plates, detected by the internal magnetic sensors, τ_{vessel}=3-4ms.

The observed heat flux striation pattern was compared with the magnetic footprint from a vacuum field line following code, calculated for the toroidal angle of the IR camera. Figure N5-7 shows that the main characteristics of the heat flux profiles do indeed follow the computed vacuum field line structure, both in the number of the observed striations, and in the relative spacing of the peaks. Note however that the precise radial locations of the peak heat flux of the lobes slightly differ from those indicated by the vacuum field line tracing.

A closer look at the structure in the heat and particle flux profiles reveals that the radial separation between consecutive lobes increases with distance from the separatrix along the divertor plate (see figure N5-7c). Note that lobes 1, 2, and 3 (the expected ones from the vacuum field line tracing, in reference to the radial location of the peak at the separatrix as the lobe number 0) appear as a combined local peak in the experimental heat flux and D_α profiles. Thus we have allocated the same value to the radial location for these three lobes in each of the heat flux and D_α profile. In general, the location of these lobes in the profiles is in good agreement with the vacuum field line tracing calculation. Finally the magnitude of the
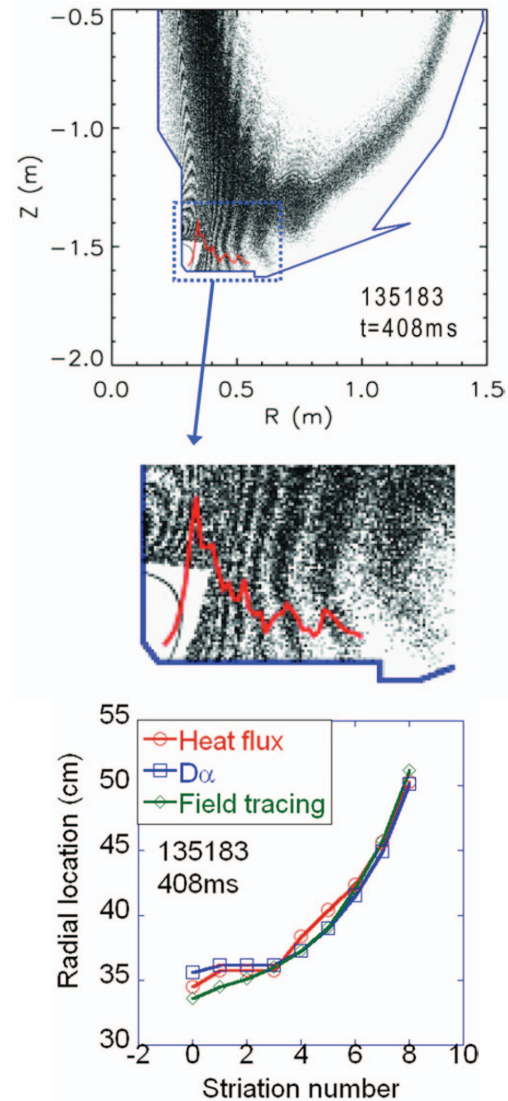

Figure N5-7: (a, b) Magnetic footprints on the divertor target, calculated by a vacuum field line tracing code for the toroidal location of the IR camera at $\phi = 135°$, with the measured heat flux profile overlaid; (c) comparison of location of striations with predictions from field line tracing [J-W. Ahn, et. al., Nucl. Fusion 50 (2010) 045010].

peaks and valleys in the IR and D_α profiles was observed to increase with increasing coil current, i.e. larger perturbing fields generated larger peaks and valleys. On the other hand, the spacing between the lobes and the lobe widths were unaffected.

The last observation we discuss is the effect of applied 3D fields on ELM heat flux. In NSTX, 3D fields are sometimes imposed to trigger ELMs in otherwise ELM-free discharges enabled by lithium wall conditioning. By increasing the applied 3D field above the ELM triggering threshold, the footprint of the ELM heat flux can be compared with the profile before the ELM but with the 3D field. Figure N5-8 shows that the triggered ELM heat flux footprint is nearly identical to the pre-ELM footprint; the ELM merely increases the intensity of the heat flux by ~ 300%.
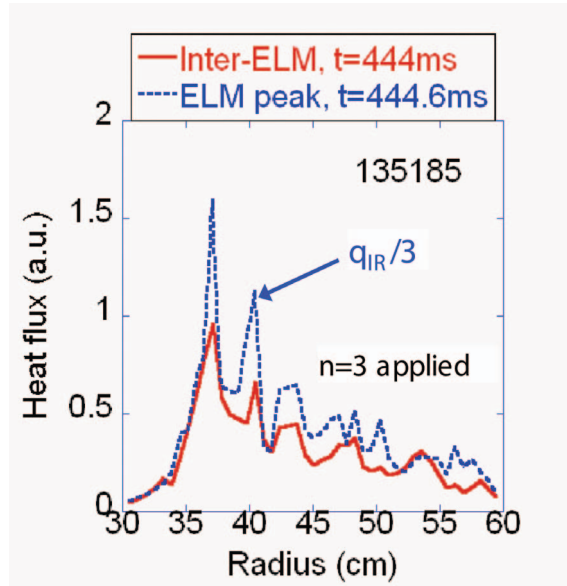

Figure N5-8. Heat flux profiles measured at an ELM peak (blue dotted line - divided by 3), and during the inter-ELM period, 0.6 msec before the peak (red solid line) To appear in J-W. Ahn, et al, J. Nucl. Mater. (2011) at press.

To summarize, intrinsic error fields and applied 3D fields clearly alter the measure heat and particle flux profiles, in a manner qualitatively consistent with vacuum field line tracing in NSTX. Looking ahead, such fields can be rotated in time to increase the time-average wetted area, which should result in reduced time-averaged temperatures and heat fluxes.

References

1. H. Zohm, et. al., *Plasma Phys. Contr. Fusion* **38** (1996) 1213.
2. A. Kukushkin, et. al., *Nucl. Fusion* **42** (2002) 187.
3. A. Kukushkin, et. al., *Nucl. Fusion* **43** (2003) 716.
4. A. Kukushkin, et. al., *Nucl. Fusion* **49** (2009) 075008.
5. R. Schneider, et. al., *Contrib. Plasma Physics* **46** (2006) 3.
6. A. Loarte, et. al., *Nucl. Fusion* **47** (2007) S203.
7. A. Kallenbach, et. al., *J. Nucl. Materials* **337-339** (2005) 381.
8. B. Lipshultz, et. al., *Nucl. Fusion* **47** (2007) 1189.
9. C. J. Lasnier, et. al., *Nuclear Fusion* **38** (1998) 1225.
10. R. Maingi, et. al., *J. Nucl. Materials* **363-365** (2007) 196.
11. R. Maingi, et. al., *Proc. 2007 Euro. Conf. on Plasma Phys. and Contr. Fusion, Warsaw, Poland, July 2-6, 2007* (2007) paper P2.020.
12. T. W. Petrie, et. al., *J. Nucl. Materials* **196-198** (1992) 848.
13. T. W. Petrie, et. al., *Nuclear Fusion* **37** (1997) 321.
14. A. Loarte, et. al., *J. Nucl. Mater.* **266-269** (1999) 587.
15. B. LaBombard, et. al., *J. Nucl. Mater.* (2010) at press.
16. C. J. Lasnier, et. al., *J. Nucl. Mater.* (2010) at press.
17. M. Makowski, et. al., *J. Nucl. Mater.* (2010) at press.
18. T. K. Gray, et. al., *J. Nucl. Mater.* (2010) submitted.
19. R. Maingi, et. al., *Proc. of 22nd IAEA Fusion Energy Conference, Geneva, SZ, 13-18 Oct. 2008* (2008) paper EX/P6-4.
20. R. Maingi, et. al., *Nucl. Fusion* (2010) submitted.
21. D. D. Ryutov, et. al., *Phys. Plasma* **14** (2007) 064502.
22. V. A. Soukhanovskii, et. al., *J. Nucl. Mater.* (2010) at press.
23. V. A. Soukhanovskii, et. al., *Phys. Rev. Lett.* (2010) submitted.
24. D. M. Mastrovito, et. al., *Rev. Sci. Instrum.* **74** (2003) 5090.
25. R. Maingi, et. al., *J. Nucl. Materials* **313-316** (2003) 1005.
26. J. W. Ahn, et. al., *Rev. Sci. Instrum.* **81** (2010) 023501.
27. A. G. McLean, et. al., *Rev. Sci. Instrum.* (2010) to be submitted.
28. H. W. Kugel, et. al., *Fusion Eng. Design* **84** (2009) 1125.
29. H. W. Kugel, et. al., *J. Nucl. Mater.* **390-391** (2009) 1000.
30. H. W. Kugel, M. G. Bell, J.-W. Ahn, et. al., *Phys. Plasma* **15** (2008) 056118.
31. D. K. Mansfield, et. al., *J. Nucl. Materials* **390-391** (2009) 764.
32. R. Maingi, et. al., *Phys. Rev. Lett.* **103** (2009) 075001.
33. T. K. Gray, et. al., *Proc. 23rd Fusion Energy Conference, Daejon, Korea, 11-16 Oct. 2010* (2010) paper EXD/P3-13.
34. S. F. Paul, et. al., *J. Nucl. Materials* **337-339** (2005) 251.
35. V. A. Soukhanovskii, et. al., *Phys. Plasma* **16** (2008) 022501.
36. V. A. Soukhanovskii, et. al., *Nucl. Fusion* **49** (2009) 095025.
37. V. A. Soukhanovskii, et. al., *Proc. 36th EPS Conf. on Plasma Physics, Europhys. Conf. Abs.* (2009) P2.178.
38. W. Fundamenski, *Private Comm.* (2010).
39. R. Maingi, et. al., *Nuclear Fusion* **45** (2005) 1066.
40. A. Herrmann, et. al. *Plasma Phys. Contr. Fusion* **37** (1995) 17.
41. D. A. Gates, et. al., *Physics of Plasmas* **13** (2006) 056122.

[42] V. A. Soukhanovskii, et. al., *Proc. 23rd Fusion Energy Conference, Daejon, Korea, 11-16 Oct. 2010* (2010) paper EXD/P3-32.
[43] M. V. Umansky, et. al., *Nucl. Fusion* **49** (2009) 075005.
[44] F. Piras, et. al., *Plasma Phys. Contr. Fusion* **16** (2009) 055009.
[45] S. A. Sabbagh, et. al., *Nuclear Fusion* **44** (2004) 560.
[46] T. E. Evans, et. al., *Phys. Rev. Lett.* **92** (2004) 235003.
[47] J. M. Canik, *Phys. Rev. Lett.* **104** (2010) 045001.
[48] T. E. Evans, et. al., *J. Physics: Conf. Series* **7** (2005) 174.
[49] M. W. Jakubowski, et. al., *Nucl. Fusion* **49** (2009) 095013.
[50] O. Schmitz, et. al., *Phys. Rev. Lett.* **103** (2009) 165005.
[51] J.-W. Ahn, J. et. al., *Nucl. Fusion* **50** (2010) 045010.
[52] J.-W. Ahn, et. al., *J. Nucl. Mater.* (2010) submitted.
[53] J.-W. Ahn, et. al., *Proc. 23rd Fusion Energy Conference, Daejon, Korea, 11-16 Oct. 2010* (2010) paper EXD/P3-01.
[54] J. W. Ahn, et. al., *Proc. 2009 EPS Conf. on Plasma Physics and Controlled Fusion, Sofia, Bulgaria* (2009) paper P2.175.
[55] V. A. Soukhanovskii, et. al., *Rev. Sci. Instrum.* **74** (2003) 2094.